A DEEP-WATER GLAUCONITIZATION PROCESS ON THE IVORY COAST–GHANA MARGINAL RIDGE (ODP SITE 959): DETERMINATION OF Fe^{3+}-RICH MONTMORILLONITE IN GREEN GRAINS

A. Wiewióra[1], P. Giresse[2], S. Petit[3] and A. Wilamowski[1]

[1] Institute of Geological Sciences, Polish Academy of Sciences, ul. Twarda 51/55, 00-818 Warszawa, Poland
[2] Laboratoire de Sédimentologie Marine, Université de Perpignan, Avenue de Villeneuve, 66860, Perpignan Cedex, France
[3] UMR 6532 CNRS HydrASA, Université de Poitiers, 40, Avenue du Recteur Pineau, 86022 Poitiers Cedex, France

Abstract—The mineral and chemical composition of green glauconitic grains from ODP Site 959 (2100 m water depth) located on the northern flank of the Ivory Coast–Ghana Marginal Ridge was studied. Recurrent winnowing of a 20 m thick Pleistocene succession resulted in a low accumulation rate and stratigraphic hiatuses. The green clay material typically occurs as fillings in the chambers of pelagic foraminifers. The amount of green clay present in sediments older than 1 Ma is small, and greater in younger material. Mud composed of smectite, kaolinite, traces of mica, calcite and quartz was the precursor material that filled the chambers of the foraminifers. Processes at the water-sediment interface slowly modified this composition. Kaolinite was dissolved; smectite lost Al but gained Fe, K and layer charge. In that matrix, the nanocrystals of neoformed smectite are observed. The infrared (IR) spectra showed OH-stretching and bending vibrations due to groups incorporating Fe^{3+}. The spectra are in agreement with the crystallochemical formulae of Fe^{3+}-rich montmorillonite as determined by point-by-point analyses on the neoformed crystallites and on the surrounding matrix. The layer charge in this Fe^{3+}-rich montmorillonite is almost wholly octahedral as shown in crystallochemical formulae and documented independently by a new IR method. The tetrahedral charge appeared when the Fe content increased by >1.2 Fe per formula unit. With the maturation process, the increased role of the closed layers is observed, with the color of grains becoming greener. We have documented for the first time glauconitization proceeding at a depth of 2100 m at a temperature near 3°C. The most important factors of the process are: accumulation of terrigenous clayey material in the foraminiferal chambers, Fe supply from a nearby continent, and a lengthy residence at the water-sediment interface in the zone of the winnowing and low sediment accumulation rate.

Key Words—Eastern Atlantic, Fe^{3+}-rich Montmorillonite, Foraminifer Fillings, Glauconitization, Green Clay, Pleistocene.

INTRODUCTION

Continuing previous work on diagenetic processes in sediments of Leg 159, Site 959 of the Atlantic Ocean Drilling Project (ODP) (Giresse and Wiewióra, 1999), this paper presents an investigation of Pleistocene green grains collected from the same sediment. The site is located on the northern flank of the Ivory Coast–Ghana Marginal Ridge, an inactive continent-ocean transform fault at a water depth of 2100 m. The green clay material fills the chambers of pelagic foraminifers. The term 'green' is used *sensu lato*. In reality, the fillings may be white, pale green, medium green, or dark green. They have accumulated mostly in the sandy fractions of the sediment, especially those related to strong winnowing actions of the water currents.

Mineralogical studies of formation of sedimentary glauconite indicated that green grains are formed initially from this same multi-mineralic material as the matrix in which they are found (Velde, 1985). Many types of substrate serve as templates for glaucony growth, but fecal pellets, carbonate tests, foraminifera and other microfossil fillings are the most common (Hillier, 1995). The initial substrates described here are

distinct from the clay fecal pellets studied previously on various continental shelves of the Gulf of Guinea (Wiewióra *et al.*, 1996, 1999). The grains of site 959 are linked to an initial clay assemblage of the mud matrix with <50% kaolinite, whereas the glauconitized fecal pellets were originally 80–90% kaolinite in the shelves.

Temperatures reported for glauconitization from low-latitude sea bottoms of the continental shelf are generally about or slightly below 15°C (Odin and Fullagar, 1988). Except for active margins where rapid subsidence could explain occurrences of green grains at depths in excess of 1000 m (Odin and Stephan, 1981), glauconitization occurs mostly between the outer shelf (below 60 m) and the upper slope (above 500 m), the optimum depth being ~200 m. The most novel feature of this occurrence of green grains at site 959 seems to be related to the low water temperature (3°C) and the water depth (2100 m) at the bottom of the site.

It is generally agreed that the degree to which the green grains have become mineralogical glauconite (a 10 Å mineral) on the continental shelves is an indicator of the length of the depositional hiatus that pro-
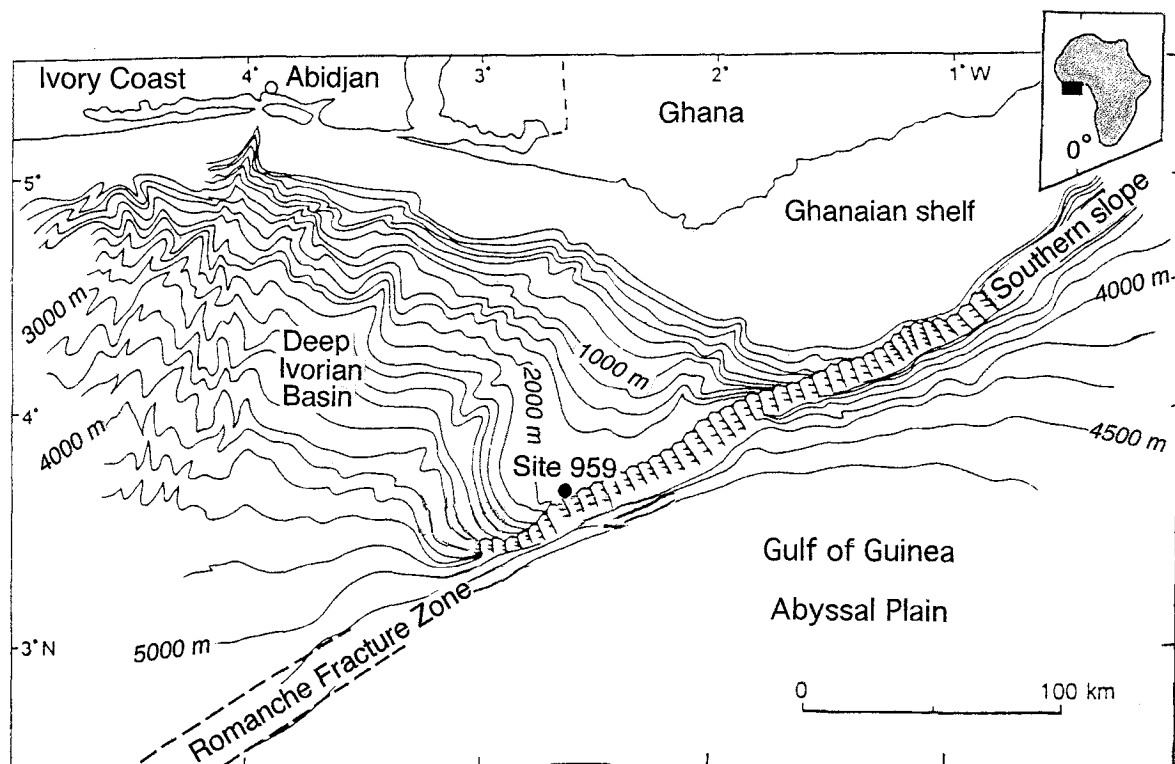
Figure 1.   Site location on Ivory Coast-Ghana Marginal Ridge.

moted its formation (Odin and Matter, 1981). Where water is deeper, energy would be lower and burial process more continuous and effective, thus inhibiting glauconitization. But deep current activity can cause winnowing of fine particles, and such reworking allows exposure of green grains at the sea-floor for periods sufficient to cause ionic exchange at the sediment-water interface.

The aim of this study is to follow the general evolution or maturity indicated by the color of the grains. A specific methodological approach was used that permitted us to study the mineralogy and chemistry of the fine-scale mineral phases and to avoid the global aspect of the analytical methods generally used in the previous studies. With a quantity of grains sufficient for analysis, the composition was determined successively by transmission light microscopy (TLM), X-ray diffraction (XRD) and by infrared (IR) spectroscopy (multigrain or single-grain scales), and by energy dispersive spectrometry (EDS) associated with a scanning electron microscope (SEM) (nano-structure scale). The IR determination of the octahedral sheet charge in the smectites helped to establish the significance of the high Fe content of the grains.

GEOLOGICAL SETTING

Hole 959 was drilled on a small plateau that extends to the north of the Ivory Coast–Ghana Marginal Ridge

(Figure 1). This margin segment is a passive transform margin, not experiencing any volcanic activity. Based on this topographic location, one would expect that the mass gravitational flow from the Ghanaian slope did not reach Site 959, but was transported into the Deep Ivorian Basin. The deposits consist of interbedded varicolored sediments (verdant green, olive brown to olive, greyish green), which generally lack sedimentary structure except for some scour contacts and bioturbation. Stratigraphic control was obtained from the oxygen isotope records, which were established on tests of the epibenthic taxon *Cibicides wuellerstorfi* (Giresse *et al.*, 1998; Wagner, 1998). This record spans the last 25 oxygen isotope stages and indicates a low accumulation rate of 1–2 cm/ka, which is three to four times lower than that recorded at nearly the same depth on the Gabonese slope (Bonifay and Giresse, 1992). Two stratigraphic intervals are missing (Figure 2): one at ~80 ka near 1.5 m below sea floor (mbsf) and another major one (520 ka) at ~11.9 mbsf. In each case, these gaps were preceded by a decreasing accumulation rate: 0.13 cm/ka at 1.5 mbsf and 0.61 cm/ka at 11.9 mbsf. These slow rates and stratigraphic hiatuses are the results of a low rate of sediment supply or pronounced bottom-current activity or a combination of the two. At 2100 m water depth, interference circulations between south-flowing North Atlantic Deep Water and north-flowing South Atlantic Inter-
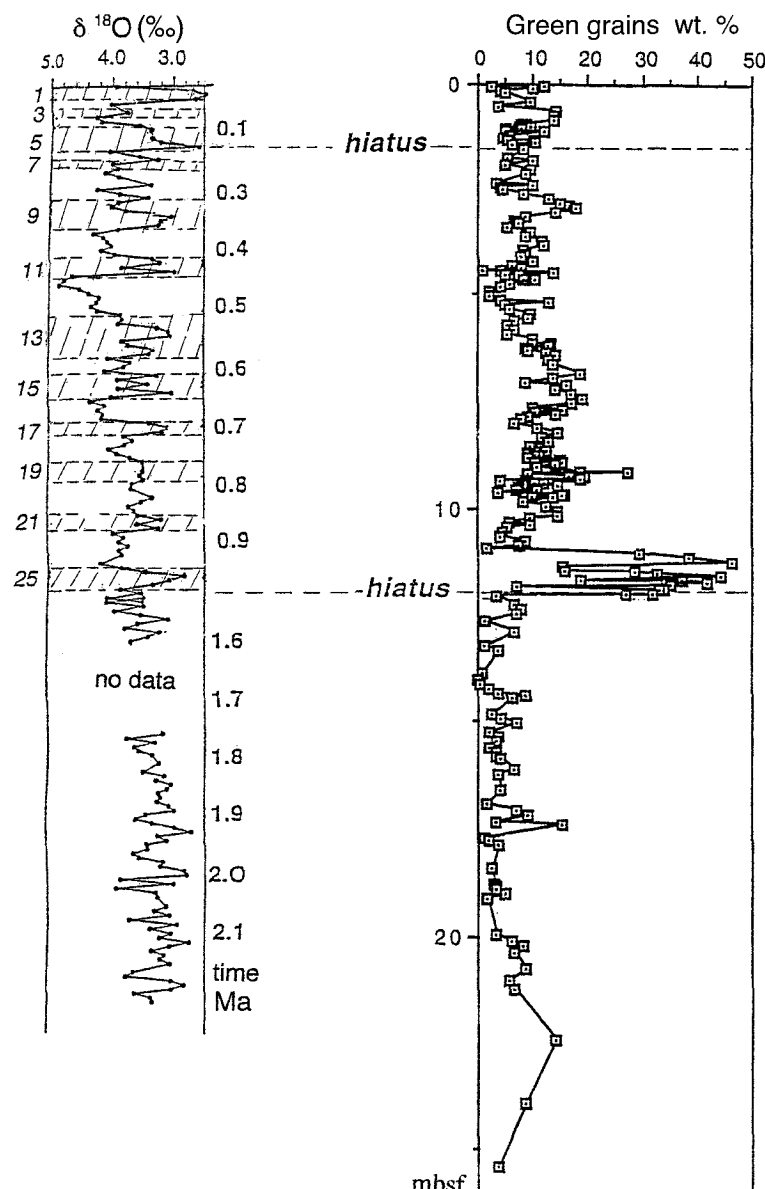
Figure 2. Down-hole profiles of green-grain contents among sand-fraction and oxygen isotope stages.

mediate Water is probably enhanced. With regard to the very steep topography along the Ridge, bottom-water velocities are especially strengthened. According to changes in the intensity of winnowing in response to variations in bottom-current velocities, a greater sand content, corresponding to larger amounts of green grains, indicates stronger bottom-water turbulence (Giresse *et al.*, 1998) as was described in Holocene upper slope sediments from Peru (Suits and Arthur, 2000).

The lithology comprises nanofossil oozes and foraminifer oozes as end-member types of sediment, with various admixtures of the two forming interbeds. Increased abundance of foraminifers gives the sediment a lighter color whereas darker layers merely have fewer foraminifers and are coccolith-enriched. Boundaries between lighter and darker intervals are gradational, usually due to bioturbation. The 11.9 mbsf scoured contact is characterized by an increased concentration of foraminifers above it.

PROCESS OF ACCUMULATION OF THE GREEN GRAINS

Some disseminated foraminifer tests are stained slightly green and dark green grains are rare. Green matter commonly fills the chambers of the pelagic foraminifers (mostly globigerine and orbuline—Figure 3) and rarely the radiole of echinids or holothurians.
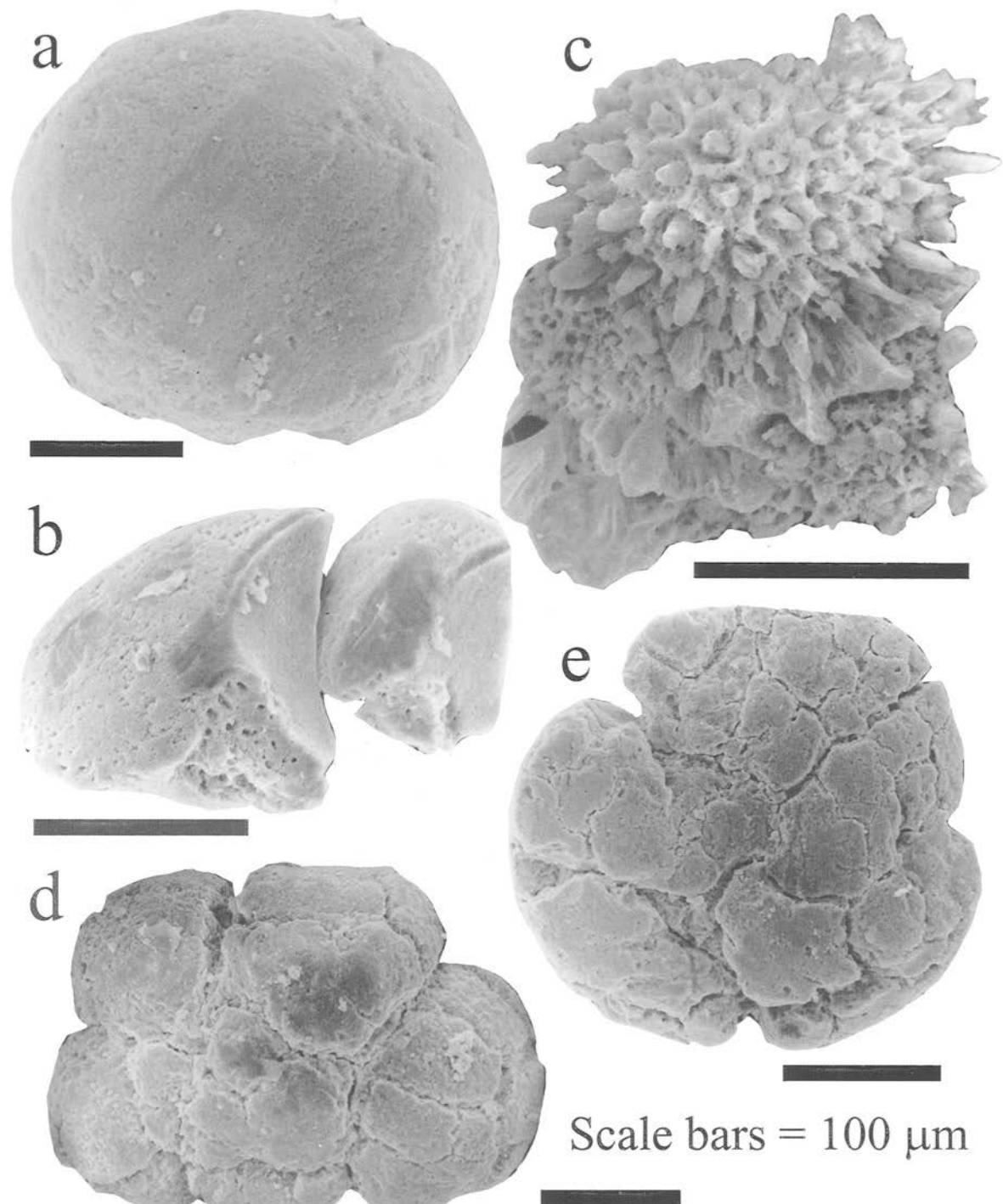
Figure 3. Morphological forms of the foraminifer fillings representing different maturation stages. a, b, c—early stages. (a) white *Orbulina* chamber filling; (b) light green *Globorotalia* chambers filling; (c) light green *Globigerinoides* filling showing white clay filling spines within the pores of the wall substrate. d, e—advanced stages. (d) dark green cracked grains; (e) darker and more cracked grain.

There is no evidence of any littoral activity in this material and it cannot be interpreted as having been transported from the top to the bottom of the slope or as being perigenic (Lewis, 1964). Ellipsoidal green fecal pellets are rare. A few pyroclastic ejecta and their diagenetic products are disseminated in some layers and their Cameroon Volcanic Ridge source was proven in a previous study (Giresse and Wiewióra, 1999).

After removal of carbonate, the residual sand fraction consists largely of the green fillings with a small proportion of pyritic framboids. Microfacies examination indicates that foraminifer fillings were partly coated by pyritic framboids (seen using TLM) as a result of late diagenetic overgrowths in reducing micro-environments. When the calcitic shells are destroyed, the framboids are released, and the green marine clays are then formed in a comparatively more oxidizing environment. This residual fraction was weighted and related to the bulk sand fraction (Figure 2). Its abundance does not appear constant with time and averages >10 wt.% especially in the lower section above 11 mbsf. The highest concentrations (20–45 wt.%) are observed around the 11–12 mbsf hiatus. The successive maxima of green-grain concentrations are not clearly linked to glacial-interglacial cycles. These concentrations and especially this 11–12 mbsf accumulation correspond to periods of slowing down of the erosional process after a long period of maximum bottom-water activity (Giresse *et al.*, 1998). Where the content of greenish grains is low, the fillings are generally white to pale green, whereas higher contents tend to be medium green to dark green and more or less split by fissures. The presence of different maturation stages in the same sample horizon provides evidence that the duration of evolution of the grains are less or more important before burial. As long as cationic exchange with the seawater reservoir is active, the proportion of highly evolved grains increases. It was concluded that a low supply of sediment and winnowing prevented rapid burial and allowed glauconitization at the sediment-water interface.

MATERIALS AND METHODS

Samples ~10 cm³ in size were taken every 5 cm (2.5–5 cm and 7.5–10 cm intervals) throughout the upper 20 m of Hole 959. After wet sieving through a 50 μm mesh, green fillings of foraminifers were readily distinguishable in the sand size-fraction with the binocular microscope. Part of this sand fraction was treated with 0.1 N HCl to remove the carbonate and to determine the percentage of the insoluble sand fraction, which consisted largely of green clay fillings (Giresse *et al.*, 1998). Further analyses were performed on another aliquot of the sand fraction using 1 N acetic acid so as to preserve the original chemical composition of the green pigment. After reaction, the acid solution was rapidly removed and the grains were washed with distilled water before drying.

The amount of green grains in the sandy fraction varies considerably, therefore the mineralogical and crystallochemical parts of the study were concentrated on levels of the core depths where green grains are most abundant (Figure 2). Starting from the water-sediment interface, the studied samples were taken at depths of 0.44, 9.44, 9.54, 10.24, 10.64–10.84, 11.74 and 14.14–14.34 mbsf. The first three samples were separated into four fractions according to color. Dark green:white grain ratios were determined for grains from the other four samples. These are 0.75 for 10.24 mbsf, 1.75 for 10.64–10.84 mbsf, 3.5 for 11.74 mbsf and <0.5 for 14.14–14.34 mbsf.

SEM/EDS

About 80 hand-picked grains were analyzed using an energy dispersive spectrometer coupled with an Hitachi scanning electron microscope. Bulk chemical data were obtained over areas of 50 × 50 μm. These analyses give a statistical approximation of the chemical composition of the variously colored grain populations. The compositions of the individual phases were obtained by spot analyses of the central parts of micro-aggregates of 2–6 μm diameter using a beam diameter of 1 μm. Analytical data were calculated on a H_2O-free basis.

XRD

A focusing transmission diffractometer equipped with a Co tube was used to study white, pale green, medium green, and dark green grains. Very small samples (~1 mm³) were studied using the Debye-Scherrer type of arrangement of the sample and a curved position sensitive detector PSD 120°2θ. The samples were analyzed in a capillary tube 0.3 mm in diameter. Changes in the *d*-value of smectite were observed before and after ethylene-glycol treatment. The Philips standard reflection diffractometer was used with a vertical goniometer equipped with a Cu tube and the scintillation counter for larger samples, such as assemblages of grains with a known dark to white ratio. The focusing reflection diffractometer with Co tube and scintillation counter was used for recording diffraction patterns of oriented aggregates of the clay fractions from the sediment muddy matrix. Diffractinel and Diffrac software were used for collection and evaluation of the diffraction patterns.

IR

A Nicolet 510 FTIR spectrometer was used to record FTIR spectra at 4 cm⁻¹ resolution in the 4000–400 cm⁻¹ range. The spectrometer was purged continuously with dry air during scanning of the transmission spectra of KBr pellets. The pellets of 13 mm diameter were prepared by mixing 2 mg samples with

150 mg KBr, to obtain well defined spectra, but with an absorbance <2. The pellets were heated at 110°C overnight to remove the adsorbed water. Integrated intensity measurements of the absorption bands were performed using the OMNIC software from Nicolet Instruments. The octahedral sheet charge of the smectites was determined by the method described by Petit *et al.* (1998). This method assumes that the total charge of smectites, as measured by CEC, is composed of the layer charge plus a variable charge due to inclusion of the crystal edge sites in the total charge. The layer charge has two components, the octahedral charge and the tetrahedral charge, both caused by heterovalent substitutions. The method is based on the integrated intensity measurement of the ν_4 NH_4 band of NH_4^+-exchanged smectites. The octahedral charge expressed in percent of the total charge, is determined by measuring the integrated intensity of the $\nu_4 NH_4$ band before and after Li fixation (Petit *et al.*, 1998). The spectra were normalized using the Si–O band near 1030 cm^{-1} as an internal reference band. Four samples characterized by different ratios of the dark green to white grains were ion exchanged by replacing the exchangeable cations with NH_4^+. Li^+ was then introduced into interlayer positions of smectite and subsequently to the vacant octahedral sites by heating overnight at 300°C (Hofmann and Klemen, 1950). The remaining layer charge was balanced by introducing NH_4^+ into interlayer space by the same procedure as previously.

RESULTS

TLM and SEM external morphology observations of the green grains

All available evidence indicates that the green fillings in the pelagic foraminifers are of deep-water origin. Some layers, <1 mm thick, contain several foraminifers filled with light green matter. Some other layers contain foraminifers filled with darker green matter. Various fillings were partly coated by a crown of pyrite framboids of late diagenetic origin. The TLM observation reveals that the green clay filled the chambers before the pyrite crystals formed. Green clay fills the well preserved pores of echinid radiole of echinids and of walls of *Globigerinoides*. Green clay also replaces the calcite walls of some foraminifers.

The SEM photomicrographs illustrate the relationship between the pelagic foraminifers and the shape of their clayey fillings. The lighter green grains (Figure 3a–c) preserve their morphology as casts of the foraminifer interiors, whereas the darker grains (Figure 3d, e) do not. The latter grains are very difficult to crush and exhibit deep cracks at their surfaces similar to those of highly evolved glauconitic grains (Odin and Matter, 1981; Giresse, 1985; Giresse *et al.*, 1988).

Mineral composition of the grains determined by XRD

A sufficient quantity of green grains for analysis by XRD was obtained from sediments most enriched in green grains. The XRD patterns (Figures 4–6) show a smectite phase that predominates over other phases. Smectite, calcite, quartz and the traces of kaolinite (Figure 4) were found in white and pale green grains from sediments at 0.44 mbsf. Little or no calcite but similar contents of quartz and kaolinite were found in white and pale green grains belonging to the deeply buried sediments. No calcite or kaolinite and only traces of quartz were observed in medium green and dark green grains (Figure 5).

As the primary material inside shells of foraminifers was derived from the surrounding mud, this sediment was separated into coarse (10–50 μm) and fine fractions. The coarse fraction consists of calcite (shells of foraminifers), quartz and a significant amount of pyrite (Figure 6). The clay fraction contains mainly smectite and kaolinite and minor amounts of calcite, illite and quartz (Figure 7).

The quantitative separation of variously colored clays from foraminifers was too labor-intensive to be performed for every sample. Therefore, we have used grain assemblages with a known ratio of the dark green to white grains for the experiments with the large quantities of material. In addition to smectites, the sample which consists mainly of white grains (ratio dark green/white = 0.75), contains calcite, quartz and kaolinite (Figure 8a), whereas the sample richer in dark green grains (ratio dark green/white = 3.5) contains very little quartz, only traces of kaolinite, and no calcite (Figure 8b).

The $d(001)$-value of non-glycolated smectite decreases with increase of the green color. It shows an interlayer spacing, $d(001)$, characteristic of smectite, of 15.2 Å in the white grains (Figure 5d). The greener the color, the lower the $d(001)$-value (Figure 5a, b). Ca^{2+} saturation of the medium green and dark green samples from 9.54 mbsf did not change the interlayer spacings of the smectite layers in the dark green grains, and modified them only slightly in the medium green grains (13.6–13.3 Å). All grains swell upon glycolation, with a $d(001)$-value of 17.1 Å (Figure 9), but the other 00l orders do not correspond to the integral orders of this spacing (Figure 9 a–c). The series is irregular and is characteristic of a mixed-layer smectite-glauconite ratio of 80/20 with R = 1, as shown by NEWMOD simulation (Figure 9d). The observed $d(060)$-value of the smectite phase equals 1.512 Å in all the diffraction patterns. It indicates 1.2 atoms of Fe^{3+} in the formula unit of smectite as determined from the figure in Wiewióra *et al.* (1996). The value of 1.512 Å is characteristic of glauconite (Wiewióra *et*
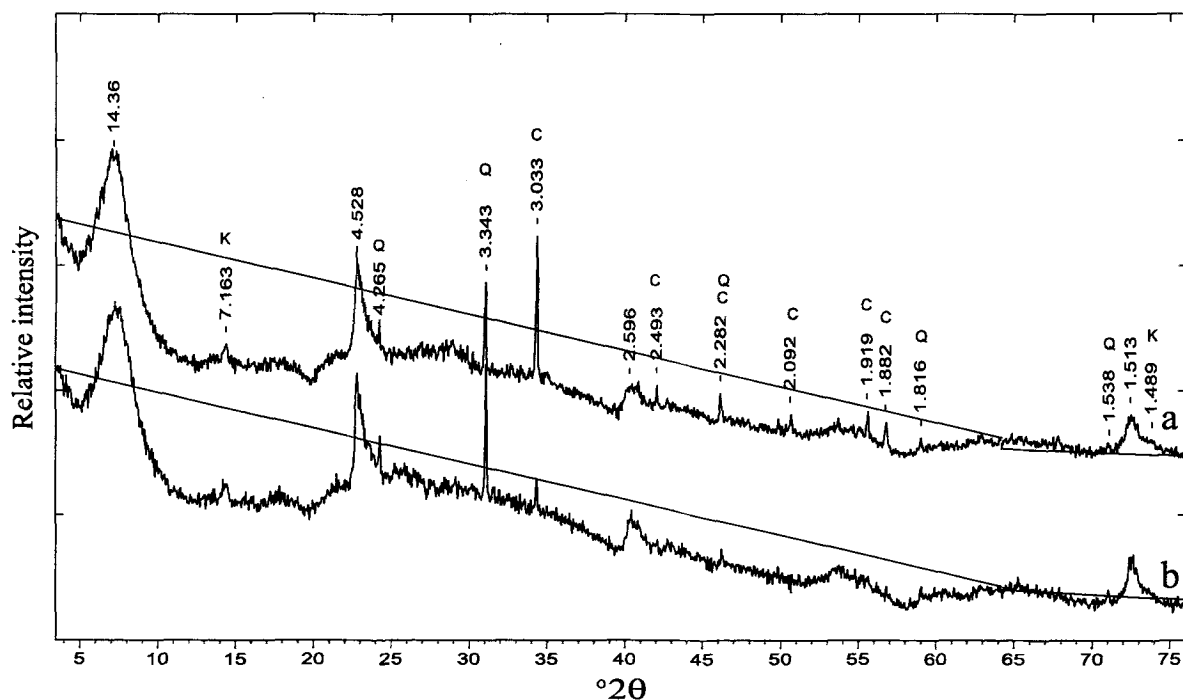
Figure 4. XRD patterns of white (a) and light green (b) grains from sediments 0.44 mbsf. The patterns were recorded using a focusing transmission diffractometer equipped with Co tube and position sensitive detector (PSD 120°2θ). K—kaolinite, Q—quartz, C—calcite, unlabeled peaks—smectite.
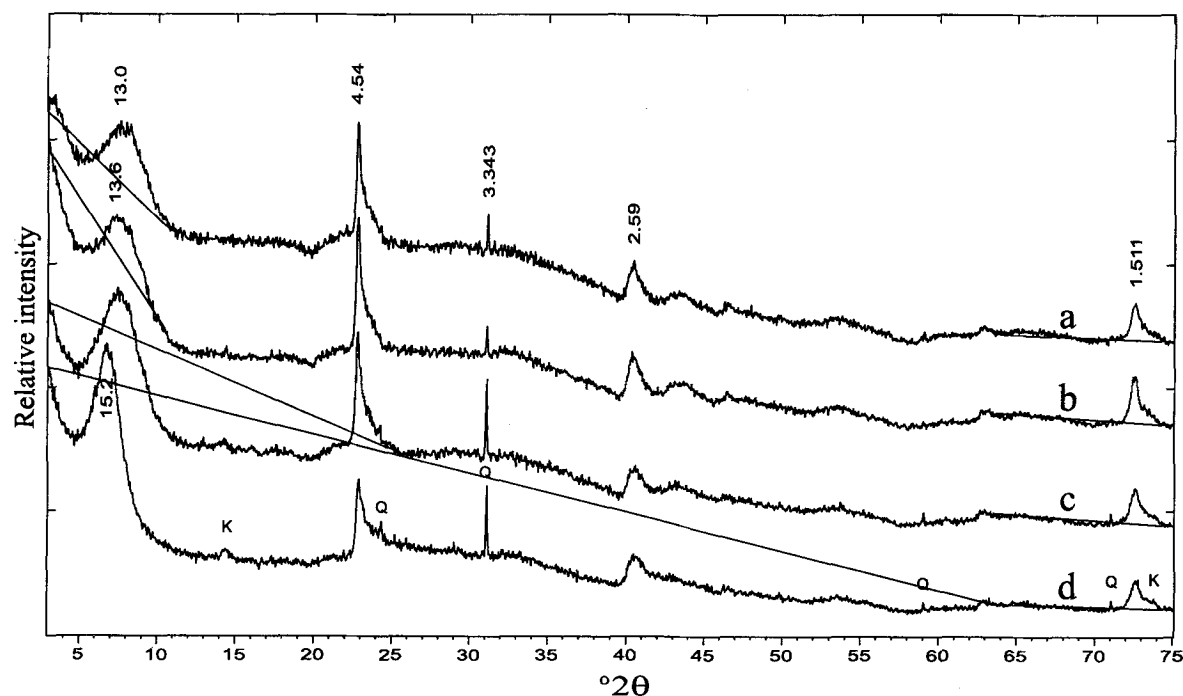
Figure 5. XRD patterns of the dark green (a), medium green (b), light green (c), and white (d) grains from sediment 9.54 mbsf. K—kaolinite, Q—quartz, unlabeled peaks—smectite. Recording conditions as in Fig. 4.
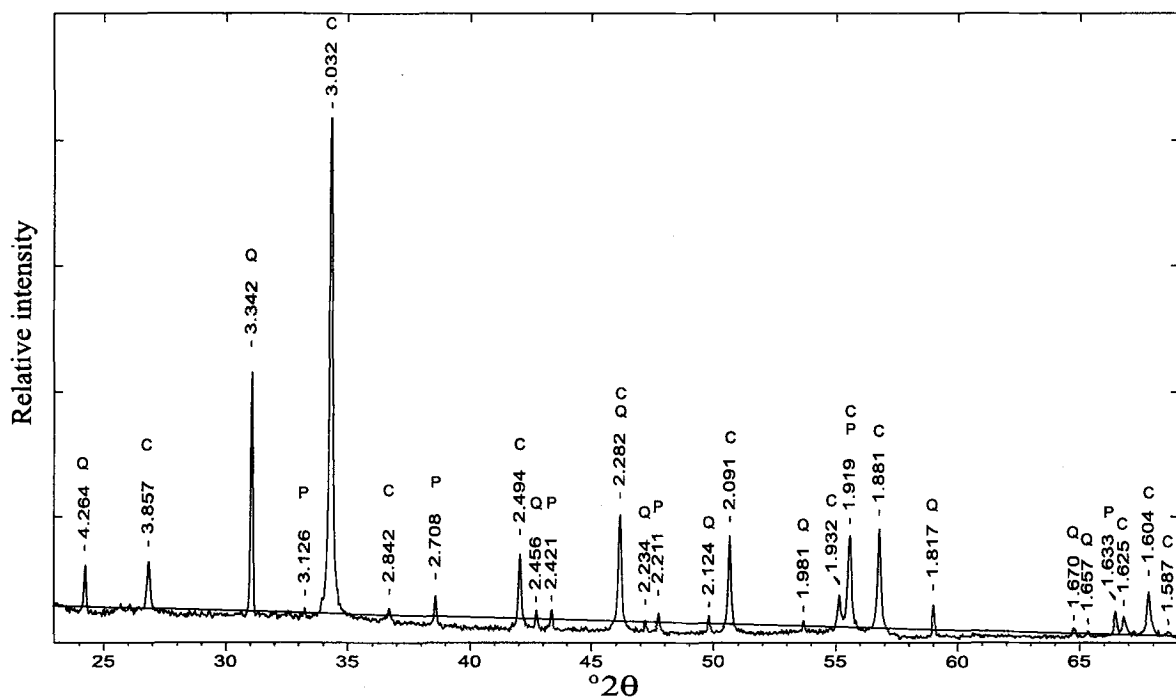
Figure 6. XRD pattern of the coarse fraction (10–50 µm) of the sediment from 9.54 m below the water-sediment interface. Recording conditions as in Fig. 4. Q—quartz, C—calcite, P—pyrite.
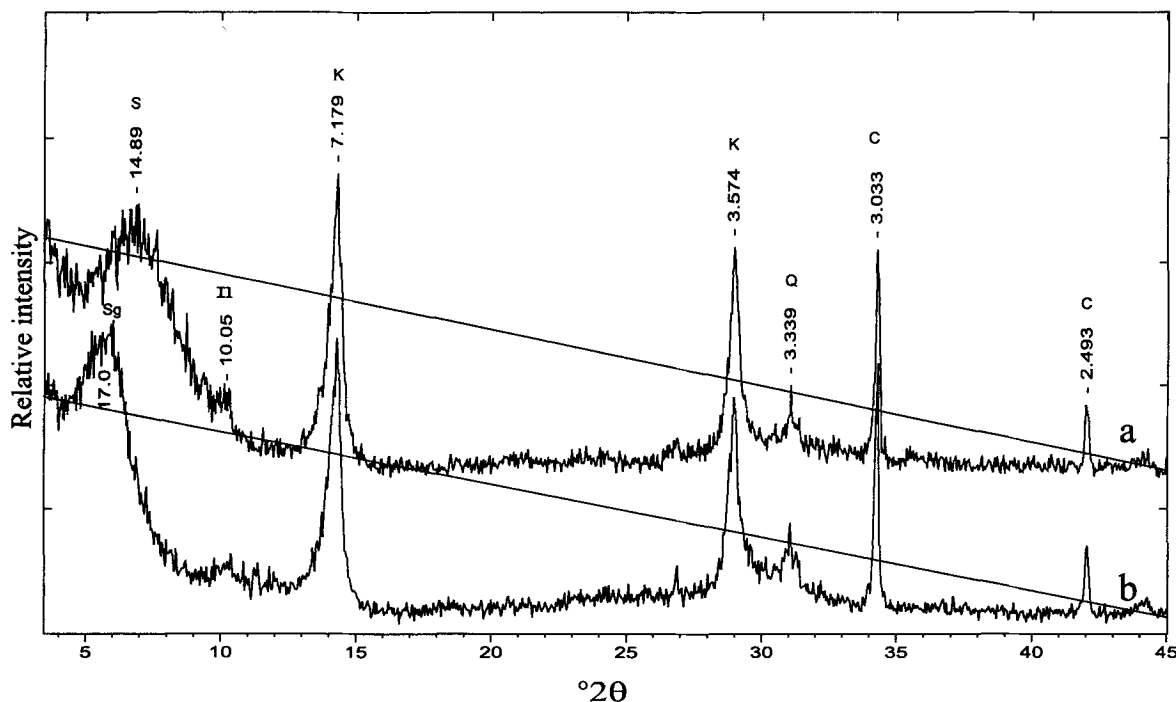
Figure 7. XRD patterns of the raw (a) and glycolated oriented aggregates (b) of the clay fraction from 9.54 mbsf. The diffractometer CGR (Compagnie Générale de Radiologie) and scintillation counter on standard, goniometer C were used. S—smectite, Il—illite, K—kaolinite, Q—quartz, C—calcite.
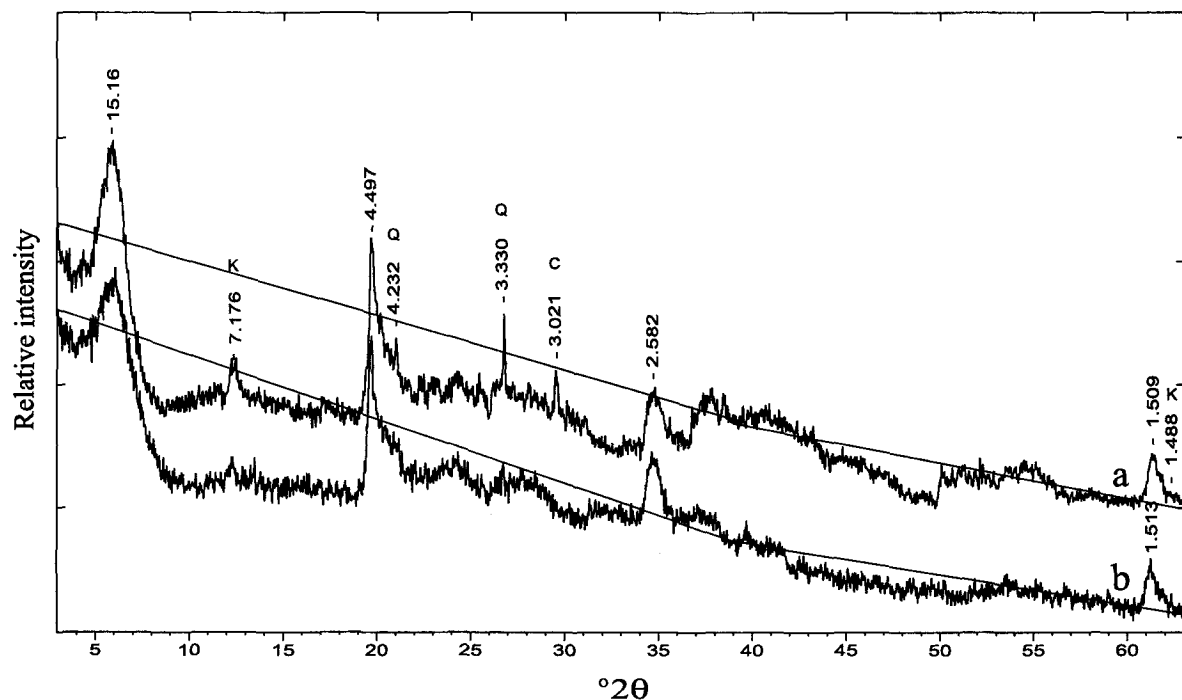
Figure 8. XRD patterns of samples with the different ratio of dark green to white grains: (a) sample from 10.24 mbsf, ratio equals 0.75; (b) sample from 11.74 mbsf, ratio equals 3.5. Diffraction patterns were recorded using CoKα filtered radiation on a standard reflection Philips diffractometer.
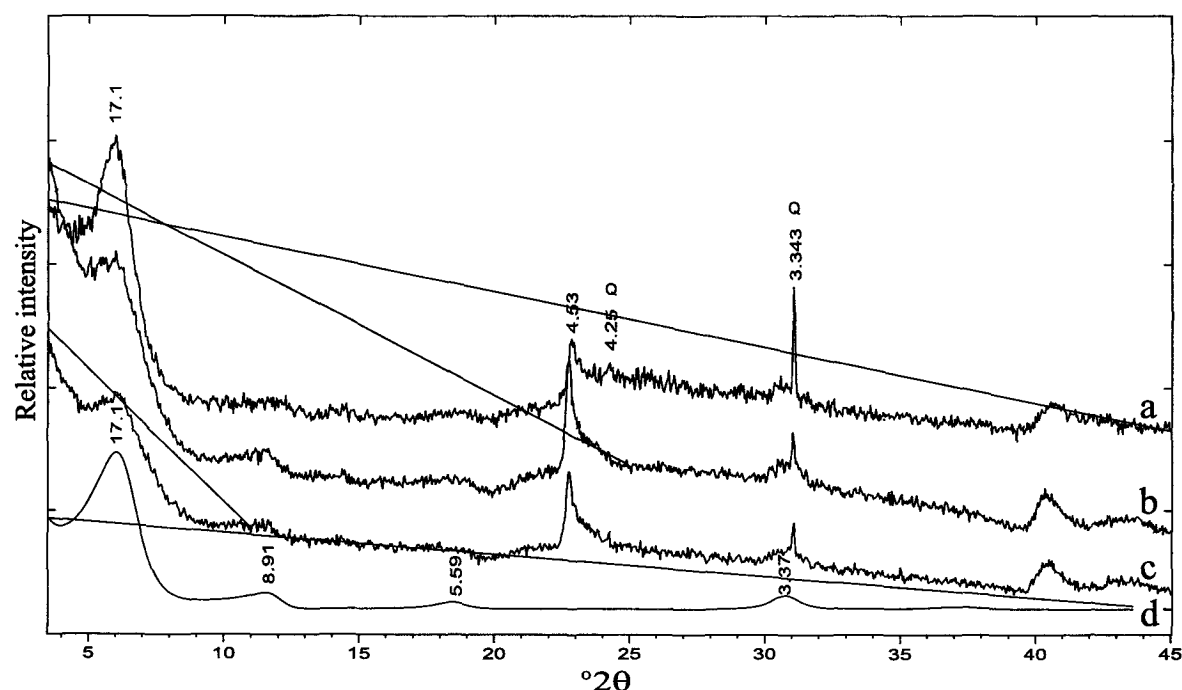
Figure 9. XRD patterns of the glycol-saturated, white (a), medium green (b), and dark green (c) grains from 9.54 mbsf. The patterns were recorded using CoKα radiation and PSD 120°2θ and compared with the calculated basal diffractions (d) using NEWMOD for interstratified 80-20 smectite-glauconite.
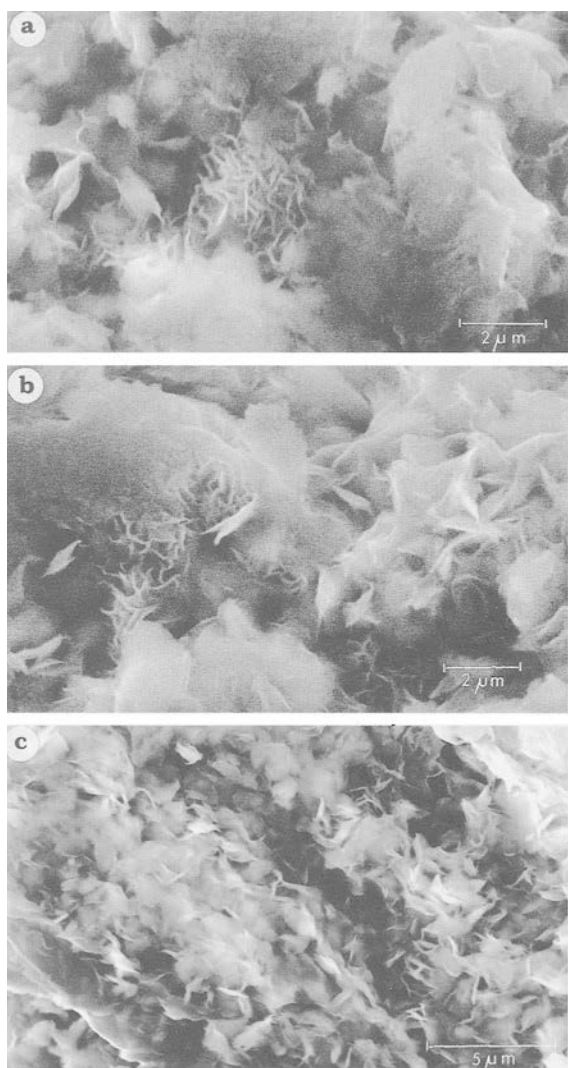
Figure 10. Scanning electron micrographs of the nano-structures and surrounding matrix inside the fillings of the foraminifers. Early stages: (a) neoformed boxwork-like nanostructures; (b) flame-like nanostructure overlapping previous nanostructures. Advanced stage: (c) high density of flame-like nanostructures.

al., 1979; Moore and Reynolds, 1989), as well as of a mixed-layer smectite-glauconite.

Morphology and chemistry of the microcrystals and of the matrix within grains

The grains from levels 9.54 mbsf and 11.74 mbsf were studied by SEM/EDS. Taking into account a high porosity, and probably a low packing density, it was easier to find neoformed nano-structures in the white grains than in the green grains. The nano-structures in small cavities seem to characterize white grains. Observations made on the grains from 9.54 mbsf are described below.

Light green grains. A first generation of neoformed nano-structures was found in the shape of more or less boxwork-like aggregates of flakes. The flakes (Figure 10a) are relatively uncommon and are ~1 μm long and 0.1–0.2 μm thick. The surface area of the aggregates is up to ~10 μm^2, larger ones (up to 50 μm^2) being rare. A later generation of flame-like nano-structures may overlap the previous ones in some samples (Figure 10b). Micrographs show flakes that are longer (~2 μm) and much wider (~2 μm) than the first ones. These second generation aggregates were found mainly in the white or pale green grains with characteristic large surface areas (~250 μm^2).

Medium green, dark green grains. The medium green grains show the same flame-like nano-structures with pronounced larger surfaces (15 × 45 μm), but they lack crystal-lined cavities. In the dark green grains, the same nano-structures were recognized. They form rather dense aggregates of well developed flakes (Figure 10c), and the aggregates have rather large surface areas (80 × 100 μm). Initially, analyses were obtained of large areas of white, pale green, medium green and dark green fillings of shells of foraminifers, including the clayey matrix (Table 1). The most important chemical elements shown by EDS analysis are Si, Fe, Mg, K and Al with some minor admixtures of Ti, Ca and Na. The white and pale green grains are rather poor in K (mean values are 2.05 wt.% and 2.67 wt.% K_2O, respectively), show irregular Fe contents and relatively high contents of Al (7.67–7.32 wt.% Al_2O_3). Higher K and Fe contents are related to medium green fillings. In the dark green fillings the K and Fe contents are highest (3.84 wt.% K_2O and 32.34 wt.% Fe_2O_3) and the Al content is low (6.32 wt.% Al_2O_3).

Although an effort was made to perform EDS analyses on the morphological forms characteristic of the smectite minerals, the large areas analyzed do not guarantee a monomineralic composition of the studied objects. Contamination by kaolinite, the second-most important mineral of the fillings, is likely. Therefore these compositions cannot be taken as the formulae of the smectite neoformed within the grain. Point-by-point EDS analyses were used to obtain better crystallochemical formulae for the microcrystals of neoformed smectite. By this method, the likelihood of contamination of these microcrystals is greatly reduced. The analyses are given in Table 2, and their crystallochemical formulae in Table 3. The data in Table 2 are arranged in samples from levels 9.54 and 11.74 mbsf. Also compared are the crystallochemical formulae of smectite in the nano-structures and in the matrix in the immediate vicinity of the nano-structures (Table 3). Formulae calculated for sample 9.54 mbsf from point-by-point analyses show little or no tetrahedral substitution in the neoformed smectite in the white, pale green or medium green grains and only a

Table 1.   Chemical data from large-area EDS analyses of white, light green, medium green and dark green grains.

	No.	SiO$_2$	TiO$_2$	Al$_2$O$_3$	Fe$_2$O$_3$	MgO	CaO	K$_2$O
White	1	51.44	0.70	7.75	34.74	1.06	2.37	1.94
	2	51.72	1.04	8.17	33.27	1.02	2.57	2.21
	3	47.65	0.30	5.26	40.19	1.04	2.66	2.89
	4	50.15	1.07	8.58	34.84	0.74	2.64	1.98
	5	48.13	0.49	6.23	39.06	0.92	2.47	2.69
	6	49.98	0.47	6.36	36.88	1.53	2.42	2.36
	7	43.32	0.70	6.64	43.26	0.88	2.97	2.23
	8	46.67	0.97	9.68	37.91	1.52	1.94	1.31
	9	44.82	0.00	4.23	44.64	0.95	2.60	2.76
	10	42.13	0.28	3.83	48.07	0.51	2.18	3.00
	11	45.49	0.86	3.39	44.12	0.94	2.03	3.17
	12	58.58	0.18	7.65	28.15	2.26	1.44	1.75
	13	62.76	0.00	7.72	22.36	3.49	1.10	2.57
	14	62.28	0.10	8.66	23.06	3.22	1.46	1.23
	15	64.19	0.22	8.42	20.10	3.97	1.04	2.06
	16	62.33	0.38	9.58	21.30	3.53	1.43	1.44
	17	63.88	0.13	6.89	22.57	3.42	1.34	1.76
	18	60.06	0.43	8.50	25.68	2.75	1.55	1.04
	19	37.09	0.55	6.26	50.11	2.79	1.28	1.92
	20	62.56	0.53	17.92	14.64	1.97	1.03	1.35
	21	50.54	0.49	7.63	36.03	2.64	1.02	1.65
	mean	52.98	0.47	7.67	32.98	1.99	1.87	2.05
Light green	22	39.22	0.42	5.90	47.59	0.95	2.55	3.37
	23	43.05	0.00	4.19	45.71	0.93	2.68	3.43
	24	46.12	0.19	3.82	42.37	1.41	2.67	3.42
	25	45.66	0.22	4.09	43.38	1.03	2.98	2.66
	26	44.99	0.40	4.38	42.49	0.88	2.07	4.79
	27	47.99	0.00	5.25	38.54	1.33	2.51	4.38
	28	44.76	0.40	4.45	42.79	0.79	1.90	4.92
	29	43.32	0.70	6.64	43.26	0.88	2.97	2.23
	30	42.41	0.34	4.03	44.93	1.45	1.92	4.92
	31	41.87	0.00	4.81	45.83	0.68	1.86	4.96
	32	44.75	0.00	3.67	43.76	1.27	2.09	4.46
	33	42.96	0.33	3.50	45.12	0.86	1.86	5.37
	34	31.67	0.25	2.93	58.53	0.66	1.51	4.45
	35	46.35	0.79	6.04	40.24	1.25	2.52	2.81
	36	45.62	0.35	5.08	42.87	0.59	2.19	3.30
	37	42.06	0.00	4.51	47.27	0.47	3.04	2.66
	38	46.87	0.00	6.69	40.16	1.22	2.85	2.22
	39	63.82	0.71	8.35	20.06	4.22	1.13	1.71
	40	63.88	0.13	6.89	22.57	3.42	1.34	1.76
	41	60.06	0.43	8.50	25.68	2.75	1.55	1.04
	42	56.91	0.00	6.91	29.71	3.39	1.74	1.34
	43	62.94	0.12	7.55	22.54	3.79	1.70	1.36
	44	63.00	0.47	9.72	20.86	3.15	1.68	1.11
	45	62.37	1.18	23.46	8.93	1.56	1.50	1.01
	46	59.62	0.00	5.53	27.22	2.92	1.11	3.61
	47	63.41	0.00	8.98	22.75	2.75	0.38	1.73
	48	62.06	0.00	7.27	26.36	1.99	0.15	2.16
	49	63.18	0.00	8.05	23.67	2.53	0.00	2.56
	50	49.69	0.34	6.14	38.15	1.05	2.71	1.93
	51	63.06	0.35	12.48	18.09	3.74	1.03	1.25
	52	63.28	0.17	8.28	21.43	3.61	1.44	1.78
	53	70.58	0.21	12.30	12.79	2.42	0.70	0.99
	54	77.17	0.76	16.17	3.41	0.00	0.54	1.95
	55	28.81	0.00	5.82	60.17	3.54	0.79	0.87
	mean	52.82	0.28	7.32	33.29	1.90	1.72	2.67
Medium green	56	49.89	0.35	5.03	37.71	1.29	2.30	3.44
	57	43.00	0.14	4.00	46.05	1.03	2.81	2.97
	58	46.75	0.36	5.30	41.46	1.20	2.40	2.53
	59	40.06	0.80	3.01	47.47	0.60	3.34	4.71
	60	43.78	0.38	4.43	44.31	1.36	2.28	3.47
	61	38.74	0.59	4.36	50.34	0.50	2.49	2.99
	62	44.76	0.40	4.45	42.79	0.79	1.90	4.92
	63	48.95	0.00	3.46	40.15	1.02	1.79	4.63
	64	44.77	0.15	3.59	43.80	0.85	1.77	5.06
	65	42.75	0.48	3.58	47.20	0.82	2.83	2.33

Table 1. Continued.

	No.	SiO_2	TiO_2	Al_2O_3	Fe_2O_3	MgO	CaO	K_2O
	66	48.49	0.00	5.42	38.90	2.78	2.69	1.71
	67	57.38	0.10	5.70	28.69	3.13	0.97	4.02
	68	62.42	0.20	7.89	23.05	3.54	1.34	1.57
	69	60.69	0.19	6.58	26.10	2.82	1.50	2.12
	70	60.57	0.00	7.92	24.01	3.13	0.68	3.69
	71	61.23	0.00	7.49	23.43	3.44	0.92	3.48
	72	57.91	0.00	7.45	25.98	3.35	1.09	4.22
	73	62.68	0.00	8.49	20.89	4.06	1.40	2.49
	74	62.42	0.20	7.89	23.05	3.54	1.34	1.57
	75	60.69	0.19	6.58	26.10	2.82	1.50	2.12
	76	59.44	0.10	7.22	25.17	3.55	2.28	2.24
	77	58.61	0.00	7.43	25.92	3.47	1.14	3.43
	78	63.71	0.42	7.97	20.56	3.94	1.10	2.29
	79	64.32	0.41	10.31	17.89	3.77	1.02	2.28
	80	39.82	0.00	8.08	47.81	2.61	0.71	0.97
	mean	53.33	0.21	6.22	33.10	2.43	1.72	2.99
Dark green	81	49.54	0.55	6.57	36.02	1.68	2.49	3.15
	82	39.12	0.38	4.20	50.17	0.66	2.13	3.34
	83	43.26	0.00	2.98	45.32	0.91	1.43	6.10
	84	46.51	0.61	4.46	40.80	0.86	3.04	3.72
	85	39.83	0.00	3.40	47.80	1.01	2.74	5.22
	86	48.57	0.47	4.64	39.17	0.89	2.75	3.52
	87	45.23	0.00	4.04	43.06	0.91	2.31	4.44
	88	36.32	0.43	3.45	51.63	1.20	2.45	4.53
	89	46.48	0.58	4.62	38.92	1.73	2.06	5.61
	90	38.22	0.00	2.96	49.01	0.55	1.34	7.93
	91	39.09	0.00	3.76	47.95	0.64	2.09	6.46
	92	44.81	0.53	3.63	41.96	1.48	1.88	5.71
	93	64.30	0.21	9.64	19.31	3.39	1.10	2.05
	94	60.00	0.00	5.02	25.69	4.00	0.70	4.59
	95	58.51	0.00	7.80	26.42	3.37	1.41	2.49
	96	59.31	0.12	6.80	26.69	3.40	1.28	2.40
	97	62.24	0.00	6.51	23.03	3.83	1.00	3.39
	98	63.67	0.18	8.59	20.16	3.97	1.02	2.42
	99	65.67	0.00	10.01	16.18	5.40	0.80	1.95
	100	57.86	1.20	7.36	25.14	3.46	1.01	3.98
	101	62.61	0.27	8.10	21.26	4.25	0.91	2.59
	102	62.39	0.21	7.62	21.37	4.28	0.95	3.18
	103	61.33	0.29	9.19	22.11	3.70	1.10	2.29
	104	48.49	0.00	5.42	38.90	2.78	2.69	1.71
	105	57.38	0.10	5.70	28.69	3.13	0.97	4.02
	106	58.41	0.25	7.62	28.06	2.25	1.67	1.75
	107	48.01	0.22	6.03	38.83	1.74	1.73	3.43
	108	53.15	0.00	7.61	30.81	2.85	1.24	4.35
	109	57.28	0.00	8.70	25.77	2.72	1.06	4.48
	110	50.84	0.00	7.25	33.97	2.82	1.19	3.93
	111	59.46	0.00	7.65	24.13	3.11	0.73	4.91
	112	60.06	0.00	7.96	23.18	3.20	0.87	4.74
	mean	53.19	0.20	6.33	32.34	2.57	1.54	3.84
Clayey matrix	113	65.47	1.04	20.15	10.12	0.89	0.84	1.50
	114	54.56	0.48	20.67	21.83	1.44	0.28	0.74
	115	62.44	0.77	11.17	21.06	2.47	1.12	0.96
	116	63.24	0.83	24.90	8.30	1.36	0.38	0.98
	117	60.26	1.30	17.61	16.45	1.74	1.32	1.31
	118	66.89	0.00	20.14	10.64	1.08	0.16	1.09
	119	51.67	1.16	19.26	10.61	2.13	12.23	1.62
	120	40.36	0.56	8.85	40.46	2.58	2.09	2.45
	121	46.69	0.00	17.73	10.12	1.81	21.08	1.63
	122	43.76	1.15	15.39	10.60	1.78	22.82	1.84
	123	43.30	0.60	16.49	8.47	2.34	24.90	1.37
	mean	54.92	0.72	17.64	15.12	1.76	7.58	1.39

Table 2. Chemical data from point analyses of smectite in white, medium and dark green grains.

		No.	Si^{4+}	Ti^{4+}	Al^{3+}	Fe^{3+}	Mg^{2+}	Ca^{2+}	K^+
			I (level 9.54 m)						
White	n	1	56.09	0.25	8.33	26.28	4.47	1.39	3.19
		2	54.24	0.00	7.55	28.91	3.89	1.46	3.95
		3	55.44	0.15	6.77	29.31	3.83	1.78	2.72
		4	53.32	0.00	7.07	33.90	2.21	0.20	3.30
	m	5	54.32	0.17	8.55	29.50	3.62	1.94	1.90
		6	49.74	0.19	7.35	35.75	2.47	1.87	2.64
		7	55.79	0.80	8.26	26.23	4.76	1.51	2.65
		8	54.12	0.13	7.35	29.87	4.21	2.24	2.08
		9	55.05	0.53	9.62	27.27	3.55	2.25	1.73
Medium green	n	10	53.83	0.23	7.45	27.60	4.76	1.26	4.87
		11	54.34	0.00	8.33	27.10	4.54	1.86	3.83
		12	49.62	0.00	7.12	32.83	3.79	1.48	5.15
		13	55.45	0.47	7.86	26.78	4.43	1.47	3.54
	m	14	53.01	0.32	8.99	28.59	4.13	1.45	3.51
		15	51.67	0.00	7.65	30.76	3.45	0.89	5.58
		16	52.42	0.00	7.26	30.02	3.80	1.21	5.29
Dark green	n	17	48.79	0.00	7.11	32.75	3.64	1.40	6.31
		18	47.96	0.11	5.40	35.93	3.38	1.24	5.97
		19	49.29	0.44	7.10	32.04	3.80	1.31	6.02
		20	50.32	0.00	7.39	30.56	3.40	0.94	7.38
	m	21	53.39	0.00	6.32	29.57	4.24	1.31	5.17
		22	50.39	0.13	6.54	33.93	3.73	1.66	3.62
			II (level (11.74m)						
White	n	23	50.60	0.00	4.81	37.83	1.95	1.71	3.10
		24	51.59	0.00	5.56	35.39	2.55	1.50	3.40
	m	25	51.35	0.00	5.62	35.06	3.47	1.34	3.16
		26	50.01	0.00	5.46	37.91	2.20	1.60	2.82
		27	52.98	0.00	5.89	34.61	2.23	1.53	2.76
Medium green	n	28	43.84	0.00	4.55	42.87	1.87	1.74	5.13
		29	50.05	0.00	5.52	35.38	2.35	1.54	5.16
	m	30	50.46	0.00	7.48	33.25	3.06	1.60	4.15
		31	51.55	0.00	5.51	34.72	2.80	1.39	4.03
Dark green	n	32	48.91	0.00	4.39	36.80	3.17	1.09	5.63
		33	48.93	0.00	4.36	36.84	3.40	1.04	5.43
	m	34	49.38	0.00	3.98	36.86	3.08	1.14	5.56
		35	47.26	0.00	4.20	39.29	2.58	1.34	5.33

n—nanocrystals, m—matrix.

little more tetrahedral substitution in the smectite from the more mature dark green grains. Other features that illustrate the maturation process from white to dark green grains are: the systematic increase in the Fe and K contents and the increase in the smectite layer charge. The same pattern exists at level 11.74 mbsf although the Fe content is greater. It should be stressed that the formulae characteristic of the three maturation stages are all Fe^{3+}-rich montmorillonite. Fe^{3+} is the major ion in the octahedral sheet. Most layer charge comes from this sheet, the tetrahedral charge being small or equal to zero. A tetrahedral charge, indicating initial glauconitization of Fe^{3+}-rich montmorillonite appears in the last stage of maturation.

IR determination of the octahedral sheet charge in smectites

X-ray diffraction analysis showed that the major component of the green grains (filling in foraminifer) is smectite. Chemical point EDS analyses proved a high Fe content in the octahedral sheet and little or no charge in the tetrahedral sheet, in spite of the structural admixture of the closed 10 Å layers (having fixed K) in the smectite structure. In the calculated structural formulae, all Fe is in the octahedral sheet, and the layer charge comes essentially from this sheet. Subsequently, Fe^{3+} cations and charge were determined in the octahedral sheet using FTIR spectroscopy.

In the OH-stretching region (Figure 11a), samples 1, 2 and 4 are very similar, with kaolinite features, as shown by the four bands at 3697, 3673, 3649 and 3620 cm^{-1}, and a broad band due to smectite centered near 3563 cm^{-1}. Sample 3 shows less intense kaolinite features and the broad band due to smectite is shifted to 3555 cm^{-1}. The position of the broad band clearly indicates that the $Fe^{3+}Fe^{3+}OH$ groups are dominant in the octahedral sites of the smectite, and thus that the smectite is very rich in Fe (Farmer, 1974). A component caused by $Fe^{3+}MgOH$ groups, the frequency of which is reported to be close to 3560 cm^{-1} (Madejová

Table 3. Crystallochemical formulae of Fe^{3+}-montmorillonites in grains of various colors from averaged point analyses presented in Table 2.

Maturation stage according to color	Nanocyrstals neoformed		Matrix inside grains around nanocrystals	
I (level 9.54 m)				
Initial (a) (white grain)	$Si_{4.02}$ $Al_{0.57}$ $Fe^{3+}_{1.09}$ $Mg_{0.31}$ $Ca_{0.06}$ $K_{0.17}$	$m = 0.30$	$Si_{3.95}$ $Al_{0.05}$ $Al_{0.58}$ $Fe^{3+}_{11.0}$ $M_{0.32}$ $Ti_{0.02}$ $Ca_{0.10}K_{0.12}$	$m = 0.32$
Middle (c) (medium green grain)	$Si_{3.96}$ $Al_{0.04}$ $Al_{0.55}$ $Fe^{3+}_{1.07}$ $Mg_{0.38}$ $Ti_{0.01}$ $Ca_{0.08}$ $K_{0.23}$	$m = 0.39$	$Si_{3.93}$ $Al_{0.07}$ $Al_{0.55}$ $Fe^{3+}_{1.12}$ $Mg_{0.33}Ti_{0.01}$ $Ca_{0.06}$ $K_{0.26}$	$m = 0.38$
Advanced (d) (dark green grain)	$Si_{3.83}$ $Al_{0.17}$ $Al_{0.38}$ $Fe^{3+}_{1.29}$ $Mg_{0.32}$ $Ca_{0.07}$ $K_{0.36}$	$m = 0.49$	$Si_{3.93}$ $Al_{0.07}$ $Al_{0.44}$ $Fe^{3+}_{1.21}$ $Mg_{0.35}$ $Ca_{0.08}K_{0.24}$	$m = 0.40$
II (level 11.74 m)				
White grain	$Si_{3.93}$ $Al_{0.07}$ $Al_{0.35}$ $Fe^{3+}_{1.42}$ $Mg_{0.20}$ $Ca_{0.09}$ $K_{0.18}$	$m = 0.36$	$Si_{3.93}$ $Al_{0.07}$ $Al_{0.38}$ $Fe^{3+}_{1.38}$ $Mg_{0.23}$ $Ca_{0.08}$ $K_{0.16}$	$m = 0.33$
Medium green grain	$Si_{3.77}$ $Al_{0.23}$ $Al_{0.19}$ $Fe^{3+}_{1.59}$ $Mg_{0.20}$ $Ca_{0.09}$ $K_{0.30}$	$m = 0.48$	$Si_{3.91}$ $Al_{0.09}$ $Al_{0.42}$ $Fe^{3+}_{1.31}$ $Mg_{0.26}$ $Ca_{0.08}$ $K_{0.23}$	$m = 0.39$
Dark green grain	$Si_{3.87}$ $Al_{0.13}$ $Al_{0.24}$ $Fe^{3+}_{1.47}$ $Mg_{0.30}$ $Ca_{0.06}$ $K_{0.31}$	$m = 0.43$	$Si_{3.86}$ $Al_{0.14}$ $Al_{0.20}$ $Fe^{3+}_{1.53}$ $Mg_{0.26}$ $Ca_{0.07}$ $K_{0.31}$	$m = 0.45$

et al., 1994), should also be recognized in this band, in addition to the $Fe^{3+}Fe^{3+}OH$ groups. After Li-treatment, the increase in intensity of the 3649 cm^{-1} band, due entirely to kaolinite before Li-treatment, is caused by the appearance of a new band near 3650 cm^{-1}, which is assigned to $\nu Fe^{3+}MgLiOH$ (S. Petit, pers. comm., 1999). This new band confirms the presence of Li^+ in the previously vacant octahedral sites of the
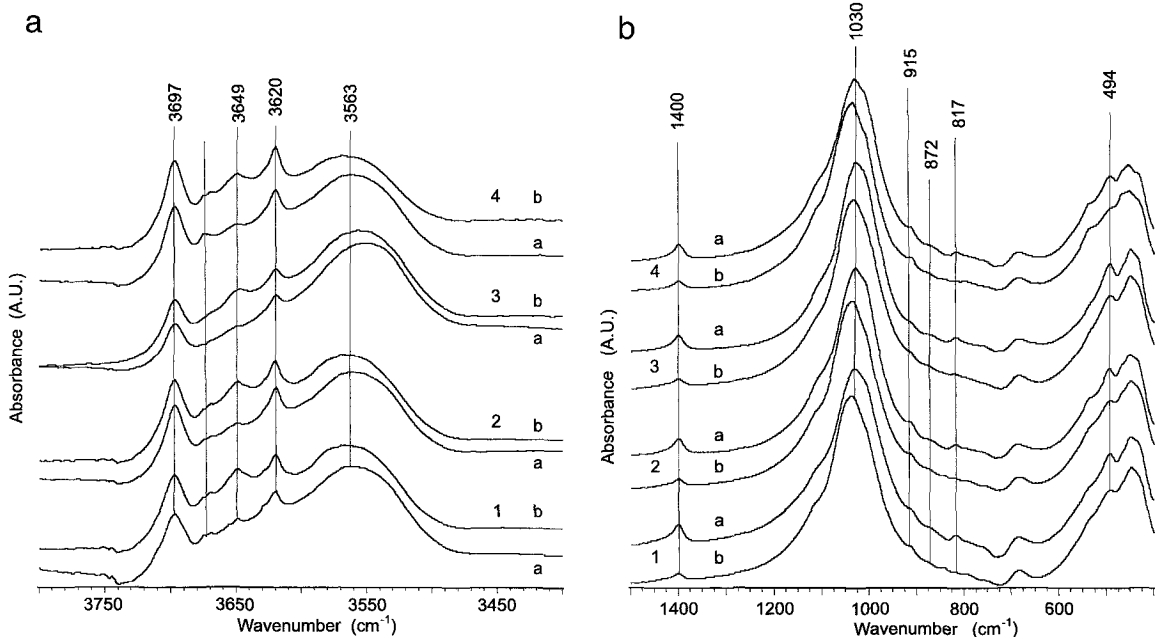

Figure 11. FTIR spectra in the OH-stretching region (a), and bending vibrations (b), of the samples with dark green:white grains ratios of 0.75 (1), 1.75 (2), 3.5 (3), <0.5 (4). (a) Sample NH_4^+ exchanged; (b) samples $LiNH_4^+$ exchanged.

Fe^{3+}-rich montmorillonite, Li^+ compensating the octahedral charge.

In the OH-bending region, the 915 cm^{-1} band is due to kaolinite (Figure 11b). For smectite, the more intense OH-bending vibration at 817 cm^{-1} is, in accordance with the OH-stretching region, the $\delta Fe^{3+}Fe^{3+}OH$ band. A small band at 872 cm^{-1}, due to $\delta AlFe^{3+}OH$ is also observed. Due to silica impurity near 800 cm^{-1}, the $\delta MgFe^{3+}OH$ cannot be seen.

The position of the absorption band at 494 cm^{-1} confirms the Fe-rich character of the smectite (Stubican and Roy, 1961). The main absorption band at 1030 cm^{-1} suggests that the Si-Fe^{3+} tetrahedral substitutions are be very limited, if indeed there are any (Goodman *et al.*, 1976).

The changes between spectra before and after Li-treatment in the 1200–400 cm^{-1} region (Figure 11b) are comparable to those observed for "montmorillonite" samples (Madejová *et al.*, 2000).

In Figure 10b, the $\nu_4 NH_4^+$ band is clearly observed at 1400 cm^{-1} for all NH_4^+-exchanged smectites, and decreases in intensity for all NH_4^+-saturated Li-exchanged smectites, indicating that the octahedral charge is relatively high. The octahedral charge of smectites, expressed in percent of the total charge, was measured following Petit *et al.* (1998). The differences in the octahedral charge are small. They cannot be interpreted precisely because the estimated error is ~5%. The octahedral charge for all samples is ~60% and clearly dominates the other components of the total charge. A high and varied charge is expected from the edge sites of smectite, glauconite-type layers and kaolinite. The tetrahedral charge is consequently very small or absent. This is shown in the crystallochemical formulae calculated from point EDS analyses. It is in accordance with the described changes between spectra of untreated and Li-exchanged samples (Figure 11a, b).

DISCUSSION

This study integrates petrographic and crystal-chemical data to document the occurrence of inherited and neoformed minerals, and discusses, on the basis of the geochemical relationship between the major elements, some new implications for the occurrence and genesis of deep-water green grains on an inactive ridge.

Deposition and morphology of green grains

The grains from the Atlantic Ocean sediments at the northern flank of the Ivory Coast–Ghana Ridge are represented principally by fillings of the chambers of pelagic foraminifers and consequently are accumulated in the sandy fraction. As a first step, the authors made sure that the green grains were not transported from the top to the bottom of the slope. All the evidence indicates their formation *in situ*. The ridge forms an obstacle to movement of water and induces the winnowing processes resulting from the deep (south–north) and the shallow northward water current. The winnowing action of the current caused accumulation of the filling in the foraminifer chambers. It is possible that the concentration of foraminifer tests and their fillings was favored by the isolation of the ridge from the main ferruginous supply.

Sediments from below the water-sediment interface enabled us to observe the mineral composition of grains from near the sediment-water interface to the more deeply buried ones and to follow the variation in the composition of white, pale green, medium green and dark green grains.

Under the petrological microscope, the grains range from white to green. The lighter grains are always enclosed by carbonate of foraminifer remnants. Pyrite frequently forms an irregular rim around fillings, between green grains and the calcite shells of foraminifers. The pyrite suggests that these fillings were matured under moderately reducing conditions such as those occurring through the action of sulfate-reducing bacteria. These sub-oxic, partially reducing conditions were also acknowledged in Oligo-Miocene glauconite in Australia (Kelly and Webb, 1999). Initial substrates here are distinct from dominant clay fecal pellets studied previously on various continental shelves of the Gulf of Guinea (Porrenga, 1967; Giresse, 1985; Odin and Fullagar, 1988; Wiewióra *et al.*, 1996; Wiewióra *et al.*, 1999).

The morphology fits the shape of the chambers of foraminifers (*e.g. Globorotalia*). Such grains are material inherited from the clay matrix (Figure 3) in which neoformed microcrystals of clayey material are rarely found. Consequently, it is obvious that the green authigenic clay replaces an heterogeneous mixture of clay-size material, which previously filled the chambers. So this part of the process is essentially the same as a shallow burial environment: glauconitic fillings of the Oligo-Miocene Torquay Group (Australia) consist of interstratified glauconite-smectite. Chemical components derived primarily from argillaceous matrix material (Kelly and Webb, 1999). More mature grains are usually cracked. Inside them the neoformed microcrystals of different generations are more abundant (Figure 3).

Mineralogy of green grains

X-ray diffraction studies of the muddy matrix showed that the fraction (10–50 μm) is composed of calcite (shell debris), quartz and pyrite (observed under the TLM and in XRD tracing) while in the clay fraction, smectite and kaolinite predominate over the traces of the illite, calcite and quartz. The relative abundance of the clay mineral assemblages is in good agreement with various previous studies (Biscaye, 1965; Griffin *et al.*, 1968; Bowles, 1975). We presume
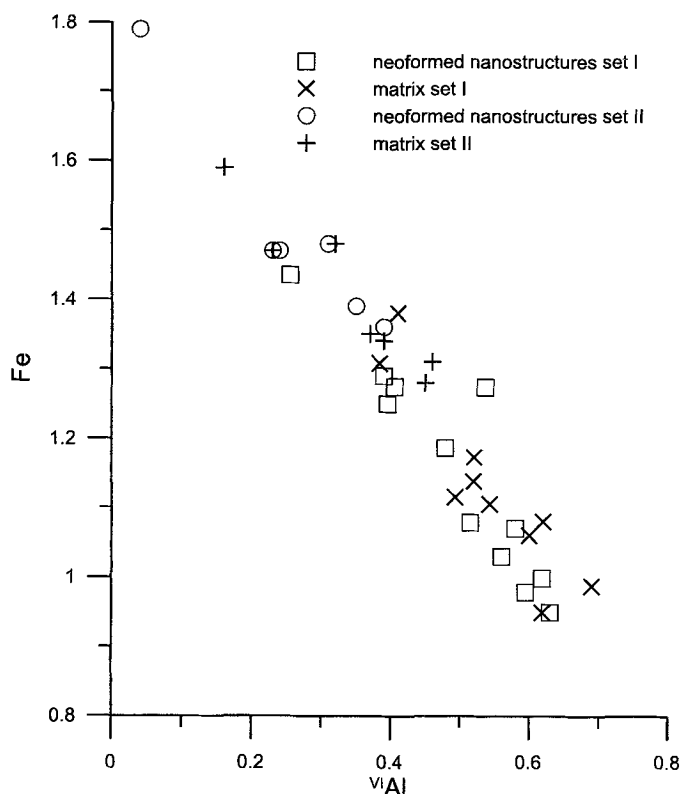
Figure 12.   Relationship between Fe and octahedral Al using recalculated data from Table 2 per half formula unit (*i.e.* $Si_4O_{10}(OH)_2$).

that this clay fraction of the sediment matrix was the precursor material that filled the foraminifers' chambers.

Apart from the initial smectite-rich composition, the common steps of the process are nearly the same as in near-surface offshore locations. These materials were modified progressively over a long time span at the water-sediment interface. Kaolinite was dissolved slowly, with remnants of $d(001)$ and $d(060)$ peaks of kaolinite in the white grains. These peaks can hardly be seen in the pale green grains but they are absent in the medium and dark green grains. Infrared spectra show kaolinite and smectite in the white to medium green grains but no kaolinite in the dark green grains, as in XRD analysis. Smectite was modified along with this dissolution of kaolinite. It is best visualized in a decrease of the $d(001)$ peak, commonly from 15.2 Å for the white grains, to 13 Å for the dark green ones. Although all of the smectites responded well to ethylene glycol, the non-integral series of basal diffractions prove that their interstratified structure consists of expanding and non-expanding layers: smectite-glauconite in an 80/20 ratio. The $d(060)$-value of 1.512 Å value is typical of glauconite but also indicates ~1.2 Fe in the smectite component. It should be stressed that the Fe^{3+} content in the crystallochemical formulae

from the EDS point analyses is ~1 Fe (white to the medium green grains) to 1.3 Fe (dark green grains) for the 9.54 mbsf level and larger for the 11.74 mbsf level. The increment in Fe content from white to green grains is associated with decrease of Al from the white to green grains (Figure 12). The other characteristic chemical features of the smectitic microcrystals of the neoformed nano-structures (Table 3) are: (1) no tetrahedral substitutions in the white grains, whereas the tetrahedral charge is ~0.2 in the dark green grain; (2) dominant contribution of the octahedral charge to the total layer charge, confirmed by an independent FTIR experiment; (3) continuous increase in the layer charge from 0.30 for white to 0.49 for the dark green grains; and (4) continuous increase in K content from the white to green grains (from 0.17 to 0.36 per formula unit).

The color of the green grains may vary from a pale green to a very dark green. There is a general indication of evolution or maturity given by the color, the lighter green material being less evolved. Generally, the color of glauconite is related to the Fe^{3+} content, with more Fe^{3+} resulting in deeper shades of green. In these Fe^{3+}-rich montmorillonites, the Fe^{3+} content generally stays below 1.5 per formula unit. In one case it reached 1.79 Fe per formula (Figure 13). This last fig-
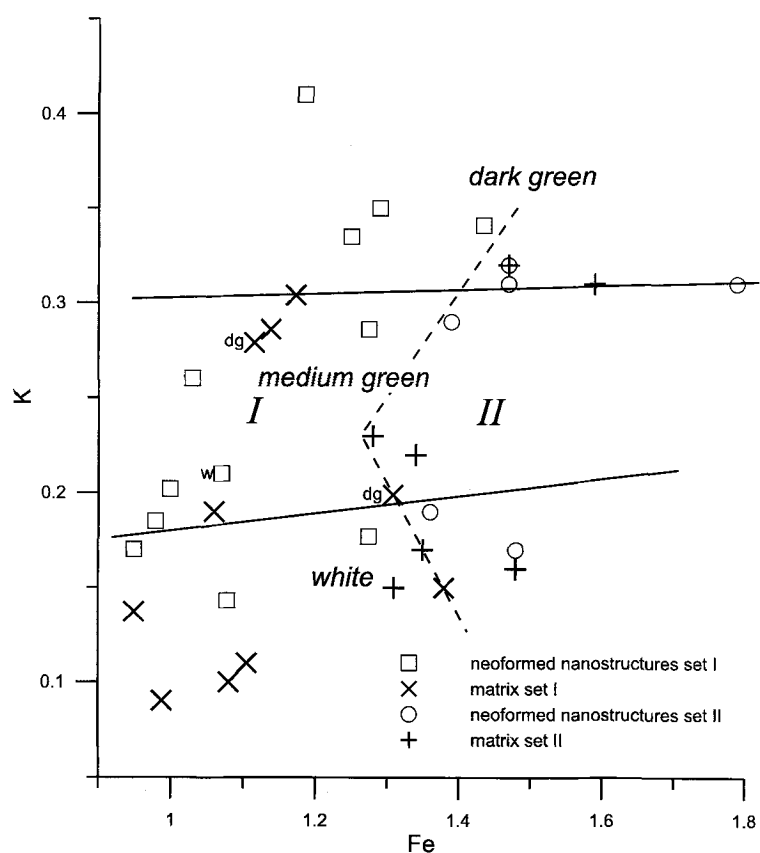
Figure 13.   Relationship between K and Fe using recalculated data from Table 2 per half formula unit.

ure clearly demonstrates that the Fe^{3+} content may not be the decisive coloring factor, as division into white, medium green and dark green assemblages correlates much better with K content. The dark green grains generally have >0.3 K per formula unit and more 10 Å layers, as determined by XRD. Thus the intensity of the green color is related to the steps of the glauconitization process.

Significance of Fe^{3+}-rich montmorillonite

Fe^{3+}-rich montmorillonite is a rare smectitic phase. It was not discussed by the different authors who worked on the green pelloids of the Gulf of Guinea shelves where nontronite is frequently observed. Amouric (1990) and Amouric and Parron (1992) referred to this mineralogical evolution from smectite to glauconite as the "montmorillonite way", distinct from that for beidellite. In the less mature grains studied (white to medium green) the smectite is represented by Fe^{3+}-rich montmorillonite. The rebuilding of the octahedral sheet, in which Fe continuously substitutes for Al (Figure 12) and where the K content also increases (Figure 13), is observed in the nano-structures and in the surrounding matrix. This shows that glauconite formation proceeds via crystallization of

nanocrystals of several, progressively more mature stages. There cannot be any ambiguity concerning the oxidation state of Fe. The IR spectra showed in both the OH-stretching and bending vibration regions, the bands due to Fe^{3+}Fe^{3+}OH groups. Additional bands due to Fe^{3+}MgOH groups and due to Fe^{3+}MgLiOH groups (after Li saturation) were found in the stretching region, and due to AlFe^{3+}OH in the bending region. Thus, the IR spectra are in a full agreement with the crystallochemical formulae determined by point-by-point analyses of the neoformed Fe^{3+}-rich montmorillonite. This validates the results obtained by both techniques (Drits *et al.*, 1997). Initially, the contribution of the closed layers to the chemistry of smectite is small. The amount of closed layers increases in the maturation processes as demonstrated by the increases in K content and layer charge. Some tetrahedral charge appears in the most advanced stage observed here, and smectite shows more clearly its mixed-layer smectite-glauconite character. A glauconitic type of non-expanding component is supported by the d(060)-value of 1.512 Å in all the samples studied.

An interesting by-product of this paper is proof that the highly ferric smectite may have only octahedral sheet charge. Crystallochemical formulae (Table 3) of
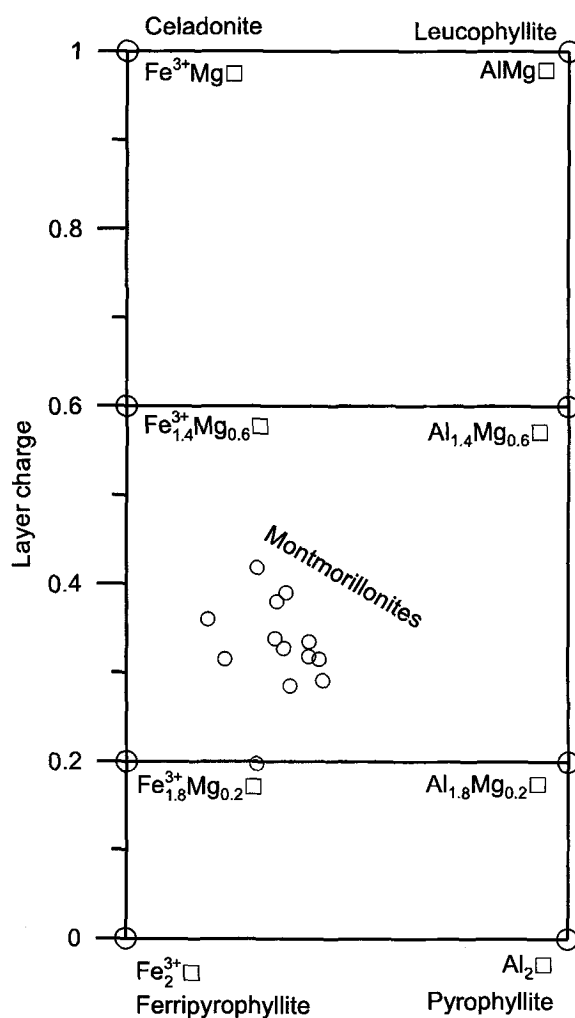
Figure 14. Projecting field for Fe^{3+}-rich montmorillonites without tetrahedral substitution using octahedral composition per $Si_4O_{10}(OH)_2$ □-vacancy. 13 projecting points come from recalculated data presented in Table 2.

Fe^{3+}-rich montmorillonites without tetrahedral substitutions are projected in the field composed of four endmembers: pyrophyllite, ferripyrophyllite, leucophyllite and celadonite (Figure 14). In all these Fe^{3+}-rich montmorillonites the Fe content is <1.3 in structural formulae. According to Drits and Kossovskaya (1980), the Fe^{3+} content for nontronite should be >1.2 per formula unit. In our last stage of maturation, not represented in the figure, the Fe^{3+} content exceeds this value. The appearance of tetrahedral substitution indicates partly nontronitic and/or glauconitic character of the Fe^{3+}-rich montmorillonites studied in this stage of maturation.

There are apparent differences between the shelf and the deep-seawater smectitic evolution, but we have focused on only a few samples of the Pleistocene deposit. The starting high-smectite content involved

suggests a possible specific glauconitization process. However, the Fe^{3+}-montmorillonite might also suggest of a process implying the mechanical dispersion of Fe^{3+} controlled by deep-water winnowing conditions.

CONCLUSIONS

The most important factors of this glauconitization are accumulation of the primary material containing montmorillonite of continental origin in the foraminifer chambers and Fe supply in a form of fine suspended material from the nearby continent. The fillings accumulated in the zone of the winnowing and low accumulation rate stayed a long time in the water-sediment interface. The conditions were favorable to the diagenetic changes of the mineral composition of clay fraction and chemical and structural changes of the smectitic component of the fillings. Therefore, in so far as comparisons with previous works using mostly global analyses are possible, the proven glauconitization steps are not markedly different from those observed in near-surface locations. The semi-confined microenvironments of the grain and the overall abundance of Fe in the sedimentary accumulation occur in tropical latitudes whatever the water depth; the continental shelf or upper-slope bathymetry are not prerequisites as long as the grains are in contact with seawater. The particular Fe^{3+}-rich montmorillonite formation might be considered as a specific process of the most winnowed deposits of the site. It was never proven in the near-shore deposits of the Gulf of Guinea.

REFERENCES

Amouric, M. (1990) La transformation gel-smectite-glauconite. Pp. 450–461 in: *Matèriaux Argileux; Structure, Propriétés et Applications* (A. Decarreau, editor). Société Française de Minèralogie et de Cristallographie, Paris.

Amouric, M. and Parron, C. (1992) About the glauconitization process. An HRTEM and microchemical study. *Proceedings Mediterranean Clay Meeting, Lipari*, pp. 11–12.

Biscaye, P.E. (1965) Mineralogy and sedimentation of recent deep-sea clays in the Atlantic Ocean and adjacent seas and oceans. *Geological Society of America Bulletin*, **76**, 803–832.

Bonifay, D. and Giresse, P. (1992) Middle to late Quaternary sediment flux and post depositional processes between the continental slope off Gabon and the Mid-Guinean Ridge. *Marine Geology*, **106**, 107–129.

Bowles, F.A. (1975) Paleoclimatic significance of quartz/illite variations in cores from the Eastern Equatorial North-Atlantic. *Quaternary Research* **5**, 225–235.

Drits, V.A. and Kossovskaya, A.G. (1980) Geocrystallochemistry of the rock-forming dioctahedral smectites (in Russian). *Litologiya i Poleznye Iskopaemye,* **1,** 84–114.

Drits, V.A., Dainyak, L.G., Muller, F., Besson, G. and Manceau, A. (1997) Isomorphous cation distribution in celadonites, glauconites and Fe-illites determined by infrared, Mössbauer and EXAFS spectroscopies. *Clay Minerals,* **32,** 153–179.

Farmer, V.C. (1974) Layer silicates. Pp. 331–363 in: *Infrared Spectra of Minerals* (V.C. Farmer, editor). Monograph **4.** Mineralogical Society, London.

Giresse, P. (1985) Le fer et les glauconies au large du fleuve Congo. *Sciences Géologiques, Bulletin,* Strasbourg, **38,** 293–322.

Giresse, P. and Wiewióra, A. (1999) Origin and diagenesis of blue-green clays and volcanic glass in the Pleistocene of the Côte d'Ivoire-Ghana Marginal Ridge (ODP Leg 159, Site 959). *Sedimentary Geology,* **127,** 247–269.

Giresse, P., Wiewióra, A. and Lacka, B. (1988) Mineral phases and processes within green peloids from two recent deposits near the Congo River mouth. *Clay Minerals,* **23,** 447–458.

Giresse, P., Gadel, F. Serve, L. and Barusseau, J.P. (1998) Indicators of climate and sediment-source variations at site 959: implications for the reconstructions of paleoenvironments in the Gulf of Guinea through Pleistocene times. *Proceedings of the Ocean Drilling Program, Scientific Results,* **159,** 585–603.

Goodman, B.A., Russell, J.D., Fraser, A.D. and Woodhams, F.W.D. (1976) A Mössbauer and IR spectroscopic study of the structure of nontronite. *Clays and Clay Minerals,* **24,** 53–59.

Griffin, J.J., Windom, H, and Goldberg, E.D. (1968) The distribution of clay minerals in the World Ocean. *Deep-Sea Research, Part A,* **15,** 433–459.

Hillier, S. (1995) Erosion, sedimentation and sedimentary origin of clays. Pp. 162–219 in: *Origin and Mineralogy of Clays, Clays and the Environment* (B. Velde, editor). Springer, Berlin.

Hofmann, U. and Klemen, E. (1950) Loss of exchangeability of lithium ions in bentonite on heating. *Zeitschift für Anorganische und Allgemeire Chemie,* **262,** 95–99.

Kelly, J.C. and Webb, J.A. (1999) The genesis of glaucony in the Oligo-Miocene Torquay Group, southeastern Australia: petrographic and geochemical evidence. *Sedimentary Geology,* **125,** 99–114.

Lewis, D.W. (1964) Perigenic, a new term. *Journal of Sedimentary Petrology,* **34,** 875.

Madejová, J., Komadel, P. and Čičel, B. (1994) Infrared study of octahedral site populations in smectites. *Clay Minerals,* **29,** 319–326.

Madejová, J., Bujdak, J., Petit, S. and Komadel, P. (2000) Effect of chemical composition and temperature of heating on the infrared spectra of Li-saturated dioctahedral smectites. (I): Mid-infrared region. *Clay Minerals,* **35,** 739–751.

Moore, D.M. and Reynolds Jr., R.C. (1989) *X-Ray Diffraction and Analysis of Clay Minerals.* Oxford University Press, Oxford, New York, 332 pp.

Odin, G.S. and Fullagar, P.D. (1988) Geological significance of the glaucony facies. Pp. 295–332 in: *Green Marine Clays* (G.S. Odin, editor). *Developments in Sedimentology,* **45.** Elsevier, Amsterdam.

Odin, G.S. and Matter, A. (1981) De glauconarium origine. *Sedimentology,* **28,** 611–641.

Odin, G.S. and Stephan, J.F. (1981) The occurrence of deep water glaucony from the eastern Pacific: the result of in situ genesis or subsidence? *Initial Report Deep Sea Drilling Program* (J.S. Watkins, J.C. Moore *et al.,* editors), **66,** 419–428. U.S. Government Printing Office, Washington, D.C.

Petit, S., Righi, D., Madejová, J. and Decarreau, A. (1998) Layer charge estimation of smectites using infrared spectroscopy. *Clay Minerals,* **33,** 579–591.

Porrenga, D.H. (1967) *Clay mineralogy and geochemistry of Recent marine sediments in tropical area.* Ph.D. thesis, University of Amsterdam, Stolk-Dordt, 145 pp.

Suits, N.S. and Arthur, M.A. (2000) Sulfur diagenesis and partitioning in Holocene Peru shelf and upper slope sediments. *Chemical Geology,* **163 (1–4),** 219–234.

Stubican, V. and Roy, R. (1961) A new approach to assignment of infra-red absorption bands in layer-structure silicates. *Zeitschrift fur Kristallographie,* Bd., **115,** 200–214.

Velde, B. (1985) *Clay minerals. A Physicochemical Explanation of their Occurrence.* Developments in Sedimentology, **40.** Elsevier, Amsterdam, 427 pp.

Wagner, T. (1998) Pliocene-Pleistocene deposition of carbonate and organic carbon at Site 959: paleoenvironmental implications for the eastern equatorial Atlantic off the Ivory Coast-Ghana. *Proceedings of the Ocean Drilling Program,* **159,** 557–574.

Wiewióra, A., Lacka, B. and Szczyrba, J. (1979) Celadonite, glauconite and skolite: nomenclature and identification problems. *8th Conference on Clay Mineralogy and Petrology,* Teplice, Geologica, Karlova University, 47–58.

Wiewióra, A., Lacka, B. and Giresse, P. (1996) Characterization and origin of 1:1 phyllosilicates within peloids of the Recent, Holocene, and Miocene deposits of the Congo Basin. *Clays and Clay Minerals,* **44,** 597–598.

Wiewióra, A., Giresse, P., Jaunet, A.M., Wilamowski, A. and Elsass, F. (1999) Crystal chemistry of layer silicates of the Miocene green grain (Congo Basin) from Transmission Electron Microscopy (TEM) and Analytical Electron Microscopy (AEM) observations. *Clays and Clay Minerals,* **47,** 582–590.